Empirical Normal Mode Diagnostic Study of the GEM Model's Dynamical Core

AYRTON ZADRA

Department of Atmospheric and Oceanic Sciences, McGill University, Montreal, Quebec, Canada

GILBERT BRUNET

Department of Atmospheric and Oceanic Sciences, McGill University, Montreal, and Recherche en Prévision Numérique, Environment Canada, Dorval, Quebec, Canada

JACQUES DEROME

Department of Atmospheric and Oceanic Sciences, McGill University, Montreal, Quebec, Canada

BERNARD DUGAS

Recherche en Prévision Numérique, Environment Canada, Dorval, Quebec, Canada

(Manuscript received 15 March 2001, in final form 27 February 2002)

ABSTRACT

An algorithm based on the empirical normal mode analysis is used in a comparative study of the climatology and variability in dynamical-core experiments of the Global Environmental Multiscale model. The algorithm is proposed as a means to assess properties of the model's dynamical core and to establish objective criteria for model intercomparison studies. In this paper, the analysis is restricted to the upper troposphere and lower stratosphere. Two dynamical-core experiments are considered: one with the forcing proposed by Held and Suarez, later modified by Williamson et al. (called HSW experiment), and the other with a forcing inspired by the prescriptions of Boer and Denis (BD). Results are also compared with those of an earlier diagnosis of NCEP reanalyses. Normal modes and wave-activity spectra are similar to those found in the reanalysis data, although details depend on the forcing. For instance, wave-energy amplitudes are higher with the BD forcing, and an approximate energy equipartition is observed in the spectrum of wavenumber-1 modes in the NCEP data and the BD experiment but not in the HSW experiment. The HSW forcing has a relatively strong relaxation acting on the complete temperature field, whereas the BD forcing only acts on the zonal-mean temperature, letting the internal dynamics alone drive the wave-activity spectral cascade. This difference may explain why the BD forcing is more successful in reproducing the observed wave activity in the upper troposphere and lower stratosphere.

1. Introduction

Dynamical-core intercomparison projects have been proposed as three-dimensional tests for global atmospheric models. The objective is to assess the various numerical schemes presently used to integrate hydrodynamic primitive equations. These tests are supposed to impose as few limitations as possible, the restrictions being meant to guarantee that one single planet is being modeled, that a statistically steady state is achieved, and that the same diagnostic criteria are used to compare the various models.

In most dynamical-core experiments, the simulated planet is spherical with no topography. A forcing function is prescribed to replace the ''physics,'' that is, the detailed parameterizations of hydrologic processes, radiation, and boundary layer turbulence that are typically present in the complete model. Moisture is absent, so only the dry momentum and thermodynamical equations have to be solved. Subgrid-scale processes such as turbulent mixing and dissipation, considered as an intrinsic part of each model, are not prescribed. Model comparison is usually based on time and zonal averages of meteorological fields (winds, temperature, pressure, geopotential height) accompanied by measurements of variability (variances, covariances) and budget (energy, momentum).

This paper presents a diagnostic study of the dynamical core of the Global Environmental Multiscale (GEM) model (Côté et al. 1998a,b), run with two distinct forc-

Corresponding author address: Dr. Ayrton Zadra, Environment Canada, Division de Recherche en Prévision Numérique, 2121, Route Transcanadienne, 5e étage, Dorval, QC H9P 1J3, Canada.
E-mail: ayrton.zadra@ec.gc.ca

ings. To characterize the model's variability, we use a three-dimensional algorithm based on the empirical normal mode (ENM) analysis, in which the transient eddies are expanded in terms of basis functions, orthogonal with respect to wave activities. The fact that orthogonality is defined by dynamics facilitates the physical interpretation of this modal decomposition. We hence propose the ENM algorithm as a complementary tool for objective intercomparison studies of dynamical cores.

Two sets of model data are considered, one produced by the GEM model with the idealized forcing proposed by Held and Suarez (1994) with stratospheric modifications by Williamson et al. (1998) and the other with the prescription of Boer and Denis (1997). Applying the same algorithm to both datasets allows us to measure the extent to which the results depend on the forcing. Results from a diagnostic study of reanalysis data (Zadra et al. 2002, hereinafter Z2002 are also used to compare the model's behavior with the variability observed in the real atmosphere. We believe that these comparative studies may provide insights for further improvements of the simplified forcings used in dynamical-core experiments.

In this paper, diagnosis is focused on a subdomain of the model's atmosphere, namely, its upper troposphere and lower stratosphere. In section 2 we briefly review the ENM algorithm and the methodology; section 3 describes the configuration of the GEM's dynamical-core experiments; results are then summarized in section 4, followed by conclusions in the last section.

2. The ENM algorithm

An overview of the algorithm's strategy and some key formulas are presented in this section. A thorough description of the ENM method can be found in Zadra (2000) and Z2002.

a. Basic state and wave activities

The algorithm was designed to diagnose data in isentropic coordinates, in which the primitive equations, wave activities, and expressions of wave–mean flow interaction take their simplest form. A balanced basic state and two conservation laws, those of pseudomomentum and pseudoenergy, constitute the main pillars of the ENM method, and the associated equations are compiled below. Hereinafter $(t, \lambda, \phi, \theta)$ represent time, longitude, latitude, and potential temperature, respectively; (u, v) are horizontal components of the wind; p is the pressure; σ is the density; and q is the potential vorticity (PV).

In the unforced, conservative limit, a zonally symmetric basic state is supposed to exist, obeying the following nonlinear, dry, thermal wind and hydrostatic balance equations:

$$\frac{\partial}{\partial\theta}\left[\left(f + \frac{u_o \tan\phi}{a}\right)u_o\right] = -\frac{1}{a}\frac{\partial}{\partial\phi}\left[c_p\left(\frac{p_o}{p_r}\right)^{\kappa}\right], \quad (1)$$

$$\frac{\partial p_o}{\partial\theta} = -g\sigma_o, \quad \text{and}$$

$$\sigma_o q_o = f + \frac{u_o \tan\phi}{a} - \frac{1}{a}\frac{\partial u_o}{\partial\phi}, \quad (2)$$

where $f = 2\Omega \sin\phi$, Ω is the earth's rotation rate, a is the earth's radius, g is the gravity constant, $p_r = 1000$ hPa, $\kappa = R/c_p$, R is the gas constant, and c_p is the specific heat at constant pressure for dry air. We choose the time-zonal mean as basic state, and the algorithm measures the adequacy of this choice by testing the balance conditions above.

All fields are separated into a mean state plus anomalies, for instance, $u = u_o + u'$, where the basic wind is labeled by a ''lowercase-oh'' index and only depends on (ϕ, θ) and the disturbance wind is indicated by a prime. Wave activities appear as conserved quantities, quadratic in the disturbance fields, associated with symmetries of the linearized equations of motion. In our case, the zonal symmetry of the basic state leads to conservation of pseudomomentum, the density of which reads

$$J = \cos\phi\left(\sigma' u' - \frac{\sigma_o^2}{2\gamma_o} q'^2\right), \qquad \gamma_o = \frac{1}{a}\frac{\partial q_o}{\partial\phi}. \quad (3)$$

It contains the wave momentum (first term) and a PV or enstrophy contribution due to wave–mean field interactions. The stability field γ_o appears as the inverse rigidity of the basic state against PV oscillations. Another symmetry, the time independence of the basic state, implies conservation of pseudoenergy:

$$A = \frac{\sigma_o}{2}(u'^2 + v'^2) + \frac{\lambda}{2} p_o^{-k} p'^2 + u_o \frac{J}{\cos\phi}, \quad (4)$$

with $\lambda = R/(g p_r^{\kappa})$ and $k = 1 - \kappa = c_v/c_p$ (c_v is specific heat at constant volume for dry air.) The first two components sum to the wave kinetic energy, the third represents potential energy, and the last one is the Doppler term associated with the background wind u_o. The ENM algorithm uses pseudomomentum and pseudoenergy spectra to characterize propagation properties of the modes, as described in the following sections.

b. ENM analysis of disturbances

Transient eddies are decomposed in terms of normal modes according to the ENM technique (Brunet 1994; Brunet and Vautard 1996), which uses the scalar product defined by a chosen wave activity. The basis functions generated by this technique are interesting in the sense that ENMs approach a set of true normal modes when disturbances are of sufficiently small amplitude.

The decomposition of wind disturbances u', for example, is represented by the expansion

$$u' = \sum_{n,s} a_{ns}(t)[u_{ns}^{(1)}(\phi, \theta)\,\mathrm{cos}s\lambda + u_{ns}^{(2)}(\phi, \theta)\,\mathrm{sin}s\lambda]. \quad (5)$$

This includes a preliminary Fourier expansion in longitude, indicated by the zonal wavenumber s, followed by a decomposition in ENMs labeled by the integer n. The time series a_{ns} is called the nth principal component (PC) for wavenumber s, and $u_{ns}^{(1\,|\,2)}$ are the zonal-wind cosine|sine components of the (ns)th ENM.

The PCs are constructed according to the snapshot method [see the appendix; see also Sirovich and Everson (1992)] as orthogonal solutions of the following eigenvalue problem:

$$\sum_j \tau_{ij}^s a_{ns}(t_j) = \lambda_{ns} a_{ns}(t_i), \qquad \overline{a_{ms}(t)a_{ns}(t)} = \delta_{mn}, \quad (6)$$

and

$$\tau_{ij}^s = \left\langle \frac{\cos\phi}{2}\left[\sigma_s'(t_i)u_s'(t_j) + \sigma_s'(t_j)u_s'(t_i) - \frac{\sigma_o^2}{\gamma_o} q_s'(t_i)q_s'(t_j)\right]\right\rangle, \quad (7)$$

where $\overline{(\,)}$ = time average. The operator τ_{ij}^s is the covariance matrix for wavenumber s, constructed with the scalar product defined by pseudomomentum, Eq. (3). Pseudomomentum is chosen over pseudoenergy in the scalar product definition because it contains fewer terms, which makes it less susceptible to noise. Angle brackets $\langle\ \rangle$ indicate a spatial integral over the meridional plane, but because we are interested at present in normal modes of the upper troposphere and lower stratosphere, this is an integral over the subdomain defined by $p_o \leq 850$ hPa. Notice that τ_{ij}^s may be interpreted as the real part of a complex time-covariance operator. It can be shown that both the complex covariance and its real part can generate true normal modes in the linear limit.

Once the PCs are found, the corresponding ENMs are obtained by projection. For example, the nth normal mode of zonal wind for wavenumber s is given by

$$u_{ns}^{(l)}(\phi, \theta) = \overline{u_s'^{(l)}(t, \phi, \theta)a_{ns}(t)}, \quad (8)$$

where $l = 1, 2$ indicate the cosine and sine components, respectively. Similar formulas apply for other fields.

c. Wave activity and phase-speed spectra

For a given wavenumber s, the algorithm computes the amount of pseudomomentum J_{ns} and pseudoenergy A_{ns} carried by each mode. ENMs are ordered according to increasing values of pseudomomentum: $n = 1$ has the most negative pseudomomentum, $n = 2$ carries the second most negative value, and so on. This is the same ordering criterion used in the diagnosis of reanalysis data (Z2002), chosen for convenience. The partition of pseudoenergy and pseudomomentum into their various components, as in Eqs. (3) and (4), is also provided by the algorithm.

The ratio of pseudoenergy to pseudomomentum defines a characteristic phase speed for each mode,

$$c_{ns}^{\mathrm{th}} = \frac{A_{ns}}{J_{ns}}. \quad (9)$$

When linear theory applies, this value coincides with the normal mode's intrinsic zonal phase speed, so we call it the theoretical phase speed. Note that a positive (negative) value of phase speed corresponds to an eastward (westward) propagating mode. Note also that the theoretical phase speed is determined by the mode's spatial structure only.

Another characteristic phase speed is derived from the time series associated with each ENM: using the PC's power spectrum, the algorithm calculates the mean frequency $\overline{\omega}_{ns}$ (as defined in Z2002)[1] and the so-called observed phase speed,

$$c_{ns}^{\mathrm{obs}} = \frac{\overline{\omega}_{ns}}{sa^{-1}}, \quad (10)$$

where a is the earth's radius. Had we a freely propagating normal mode with a monochromatic power spectrum, this would be its intrinsic phase speed. However, in most situations, the observed power spectrum is polychromatic because of nonlinearities, dissipation, and external forcing, in which case c_{ns}^{obs} should be seen as a mean phase speed.

Here we will compare the theoretical and observed phase speeds of the leading ENMs. A similar approach was used by Brunet and Vautard (1996), who analyzed a forced, nonlinear shallow-water model and verified that, for some of the leading modes, the theoretical and observed phase speeds were the same.

d. Algorithm's output

The diagnosis of the model's dynamical core is based on 1) the zonal climatology of wind, pressure, specific volume, and PV in θ coordinates; 2) a complete decomposition of transient eddies in the upper troposphere and lower stratosphere in terms of ENMs and PCs for wavenumbers $s = 1$–9; 3) detailed spectra of the ENMs's pseudomomentum and pseudoenergy; 4) the power spectrum associated with each PC; and 5) the ENMs's observed and theoretical periods, derived from the phase speeds in Eqs. (9) and (10).

3. Datasets

Data are provided by two 2.5-yr-long dynamical-core experiments using the GEM model. Both were run with

[1] Here the wavenumber $s = 1, 2, \ldots$ is positive definite and the sign of the observed phase speed is determined by the sign of the mean frequency $\overline{\omega}_{ns}$.

a uniform grid of $2° \times 2°$ (nonrotated), 26 levels with a nearly uniform vertical resolution in log pressure and the roof at 25 hPa, a 3600-s time step, and neither topography nor land–sea separation, the only difference between the experiments being the simplified forcing. The first experiment applied the benchmark calculation proposed by Held and Suarez (1994) and later modified by Williamson et al. (1998); the second experiment used a forcing inspired by the prescriptions of Boer and Denis (1997).

These experiments differ essentially in the way that temperature is forced. In the Held–Suarez–Williamson (HSW) prescription, temperature is locally relaxed to a zonally symmetric equilibrium according to the formula

$$\frac{\partial T}{\partial t} = \cdots - k_T(\phi, p)[T - T_{\text{eq}}(\phi, p)], \qquad (11)$$

where dots represent internal dynamics. The restoring coefficient k_T and the equilibrium temperature T_{eq} are prescribed analytical functions of latitude and pressure, symmetric with respect to the equator. For instance, the temperature profile specified by Held and Suarez is

$$T_{\text{eq}} = \max\left\{200, \left[315 - 60\sin^2\phi - 10\log\left(\frac{p}{1000\text{ hPa}}\right)\cos^2\phi\right]\left(\frac{p}{1000\text{ hPa}}\right)^{2/7}\right\}\text{K}.$$

The stratospheric modification prescribed by Williamson et al. (1998) is also symmetric about the equator and is effective when p is less than 100 hPa.

The Boer–Denis (BD) forcing has a flow-independent heating function H_o plus a weak negative feedback on the zonally averaged temperature, as represented in the equation

$$\frac{\partial T}{\partial t} = \cdots + H_o(\phi, p) - \beta\{[T]_z - T_o(\phi, p)\}, \qquad (12)$$

where $[\,]_z$ indicates zonal mean and $1/\beta = 75$ days. Here T_o was taken as the climatological zonal reference temperature proposed by Boer and Denis (1997). The function H_o is time and flow independent, is symmetric about the equator, and was constructed using the output of a preliminary HSW experiment of the GEM model.

Only the last four months of each run were taken and then sampled at 6-h intervals and spectrally projected on a horizontal grid with 32 latitude circles and 22 meridians, which allows an analysis of synoptic scales and larger. The model data were also interpolated into θ coordinates, with 16 isentropic levels between 270 and 450 K and higher resolution in the upper troposphere.

4. Results

Diagnostic results are presented for both dynamical-core experiments simultaneously. Whenever possible, a comparison is made with the diagnosis of reanalysis data.

a. Basic-state diagnosis

Figure 1 shows the time-zonal mean of the zonal wind generated in the two experiments. With the HSW forcing (Fig. 1a), two symmetrical midlatitude jets are found, centered at latitudes $\pm 45°$ with maxima of 30 m s^{-1} near the 315-K level. The BD forcing (Fig. 1b) also provides symmetrical jets, with maxima of 28 m s^{-1} near $\pm 50°$ of latitude between the 330- and 345-K isentropes. The jets in the BD experiment resemble more the summer jet obtained from reanalysis data (Z2002) in shape, location, and intensity. The BD forcing produces a slightly stronger upper-equatorial jet, as already observed by B. Denis (2000, personal communication).

The basic pressure obtained in the HSW experiment (Fig. 2a) is characterized by three distinct domains: a bell-shaped plateau corresponding to the near-surface domain with pressures above 950 hPa, the mid- and upper troposphere with stronger pressure gradients, and a relatively isothermal lower stratosphere (Held and Suarez 1994; Williamson et al. 1998). The ENM diagnosis of variability presented in this paper is restricted to the subdomain above the 850-hPa isobar. In the BD experiment (Fig. 2b), this separation surface occurs at lower levels and the large pressure gradient band is broader than the one obtained with the HSW forcing, especially at low latitudes. A relatively broad band was also observed in the National Centers for Environmental Prediction (NCEP) reanalyses study and, in this sense, the BD forcing seems to produce a more realistic mean field. In both cases, the zonal wind is verified to be in gradient–thermal balance with pressure, as in Eq. (1), within 10%.

In Fig. 3, the mean PV fields are shown. Near the poles, the BD forcing gives more horizontal PV isolines than do the HSW experiment and analysis data. In both experiments we have found domains of negative PV gradient ($\partial q_o/\partial\phi < 0$) at lower levels, at low latitudes, indicating possibly unstable domains that were not found in the NCEP data study. These domains of negative PV gradient—not visible in Fig. 3 because of the selection of contour lines—are located in the lower regions that are eventually masked and have no direct impact on the diagnostics of the upper regions.

In the previous study on reanalysis data, the stability field normalized by density [$\gamma_{\text{qg}} \doteq \sigma_o \partial q_o/\partial(a\sin\phi)$] was shown to be a reliable indicator of regions of high wave

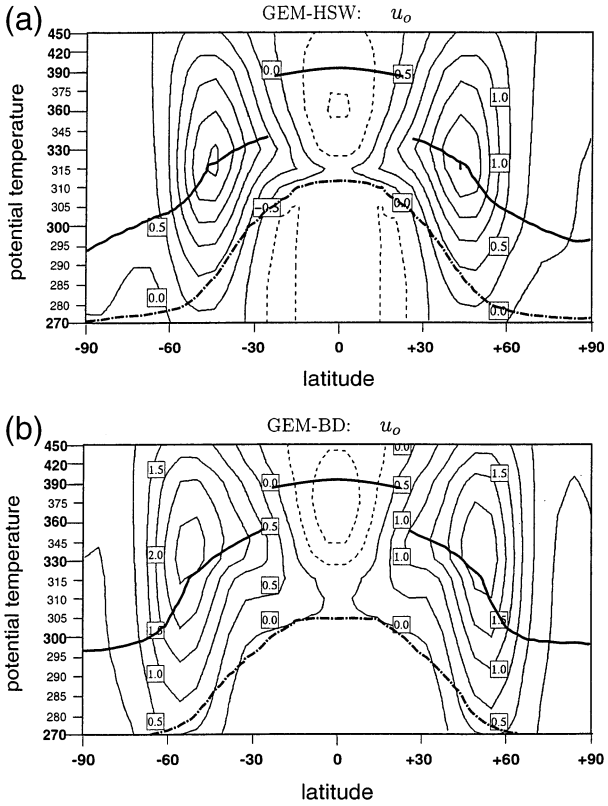

FIG. 1. Meridional cross sections showing the time-zonal mean of the zonal wind u_o ($10 \times$ m s^{-1}) generated by the GEM model using the idealized forcing of (a) HSW and (b) BD. The tropopause (marked by a thick solid line) is defined by $q_o = 2 \times 10^{-6}$ K m^2 kg^{-1} s^{-1} at latitudes $|\phi| > 25°$ and by $\theta \sim 390$ K at $|\phi| < 25°$, according to Hoskins and Karoly (1981). The separation between lower troposphere and midtroposphere is indicated by a thick dot–dash line. In Figs. 1–6, contour labels are given in boxes (the lower right corner of each box points to the corresponding contour line).

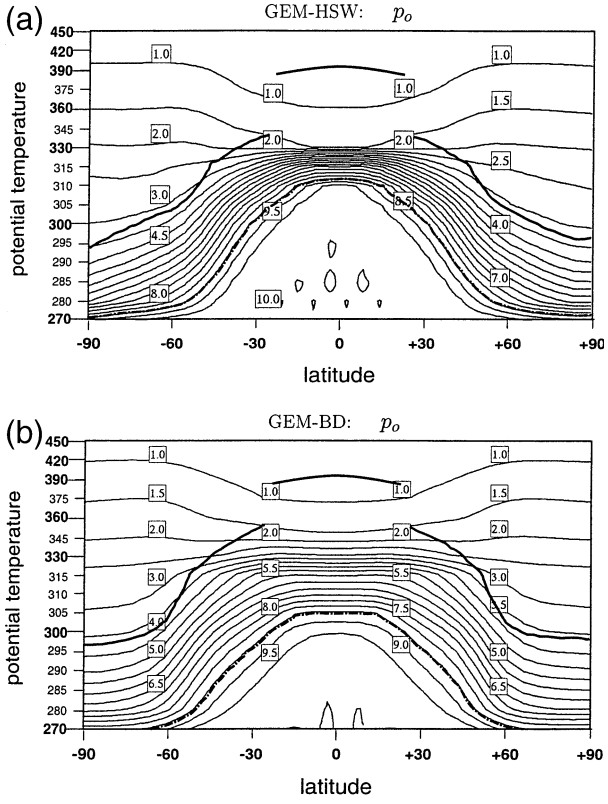

FIG. 2. As in Fig. 1, but for the pressure field p_o ($100 \times$ hPa).

activity. The same field, now generated by the model, is plotted in Fig. 4 showing the typical pair of mid- and high-latitude ridges in the upper troposphere. A plot (Fig. 5) of the time-zonal mean of quasigeostrophic wave enstrophy, defined as $[\sigma_o Q'^2]_\lambda$, with $Q' = \sigma_o q'$ and $[\bar{}]_\lambda$ = time-zonal mean, confirms that most variability occurs in the regions for which the stability field γ_{gq} is large. In the HSW experiment, however, the wave-enstrophy field exhibits a local maximum near the equator that is not found in the diagnosis of NCEP data nor in the BD experiment.

b. ENM analysis

The leading ENMs, which carry most wave activity, are characterized by relatively large scale features. Their amplitudes (not shown) are centered at high latitudes for low values of the wavenumber s and migrate to mid- and low latitudes as s increases, in agreement with previous model studies. Spatial correlations can be qualitatively understood in terms of quasigeostrophic ideas: for instance, if the meridional-wind mode is taken as a streamfunction ($v_{ns} = is\psi_{ns}$), then the zonal-wind mode can be reconstructed accordingly [$u_{ns} \approx -\partial(\psi_{ns} \cos\phi)/\partial\phi$]. These properties are common to both experiments, independent of the forcing, and are compatible with the patterns obtained with the reanalysis data.

To some extent, the ENM structures generated with both forcings are similar to the modes observed in the real atmosphere. To illustrate this property, Fig. 6 shows the leading wavenumber-5 modes of zonal wind (Fig. 6c) and pressure (Fig. 6d) obtained in the BD experiment: the dipolar structures are strikingly similar, both in shape and amplitude, to the leading wavenumber-5 ENM found in the summer hemisphere of the NCEP reanalysis study (Z2002). The characteristic phase speed of 9–10 m s^{-1} and decay rate of approximately 4 days, computed as in Z2002, compare well with the phase speed of 12 m s^{-1} and decay rate of 3 days found in the observations. In the diagnosis of the BD experiment, we also find a mirror image of this wavenumber-5 dipolar mode in the Northern Hemisphere (not shown), as expected from the symmetries of the forcing. These modes exhibit several properties of upper-tropospheric propagating quasi modes, defined by Rivest et al. (1992) and Rivest and Farrell (1992) as superpositions of singular modes sharply peaked in the phase-speed domain. The fact that they are observed as leading modes in global data and numerical models indicates that quasi

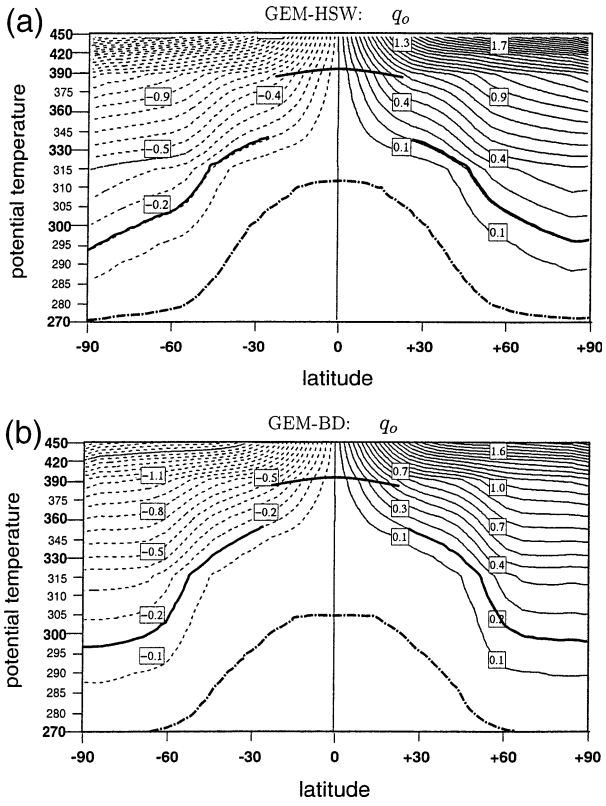

FIG. 3. As in Fig. 1, but for the potential vorticity q_o ($10^{-5} \times$ K m^2 kg^{-1} s^{-1}).

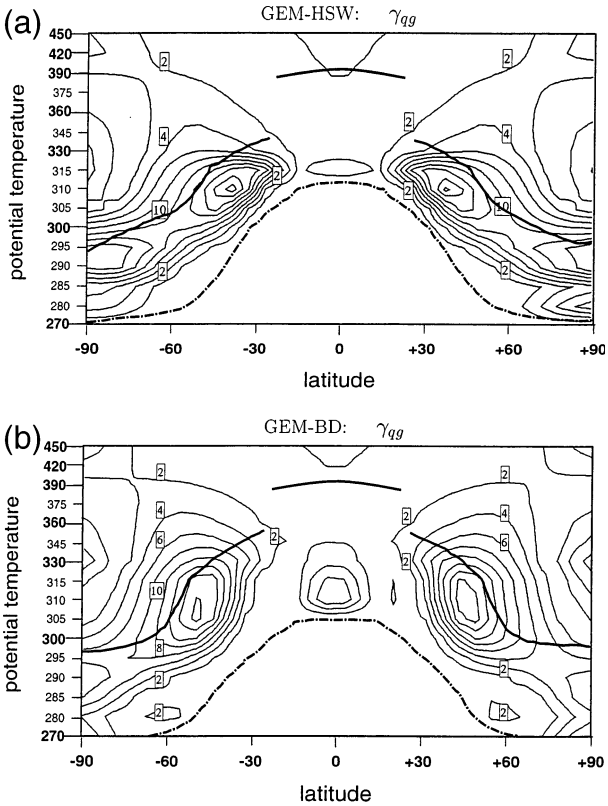

FIG. 4. Cross sections of the meridional PV gradient normalized by the basic specific volume, defining the stability field $\gamma_{qg} = (\partial q_o/\partial\phi)/a\alpha_o \cos\phi$ ($10^{-11} \times$ m^{-1} s^{-1}) (a) with the HSW forcing and (b) with the BD forcing.

modes play an important role in the upper-troposphere dynamics.

We also find a similar mode in the ENM analysis of the HSW experiment, shown in Figs. 6a and 6b. It is the third-leading wavenumber-5 ENM, with a phase speed of 7–9 m s^{-1} and a decay rate of approximately 2 days. The simultaneous dipolar structures in the Northern Hemisphere indicate that the pair of degenarate hemispheric modes have not been completely separated by the algorithm.

These results seem to suggest that both forcings are capable of generating realistic patterns of variability in the upper-tropospheric and lower-stratospheric regions. However, one could argue that this comparison of spatial structures is subjective and that the differences or similarities between ENMs might have been less evident had we used other coordinates. The following sections, containing detailed spectra of wave activities and periods, provide further and quantitative pieces of evidence to this comparison.

c. *Wave-activity spectra*

Examples of pseudomomentum and pseudoenergy spectra for wavenumber $s = 5$, obtained with the HSW and BD forcing, are shown in Figs. 7 and 8. The partition of pseudomomentum is illustrated in Figs. 9 and 10, also for wavenumber $s = 5$. Similar spectra are obtained with other wavenumbers (not shown) and, in qualitative terms, these spectra resemble those found in the diagnosis of reanalysis data (Z2002).

Leading modes reside in the small-n range (say, between $n = 1$ and 100), where pseudomomentum and pseudoenergy are large, are negative, and are dominated by the PV contribution. According to the theoretical Eq. (9), these modes should propagate eastward. Their spatial structure and wave-activity partition indicate that these ENMs are planetary vortical modes.

At the opposite extreme of the spectra, pseudomomentum and pseudoenergy are both positive. In this range, density oscillations and the associated momentum term become important. The theoretical phase speed is also positive, but the wave-activity partition suggests that wind divergence is an important characteristic of these ENMs, as opposed to those in the small-n range.

In between the two ranges above, say, for n between 200 and 400, we find ENMs carrying negative pseudomomentum and positive pseudoenergy and theoretically propagating westward. Their wave activities are many orders of magnitude smaller than those of the leading modes. The transition from the small- to intermediate-n ranges is marked by an approximate balance

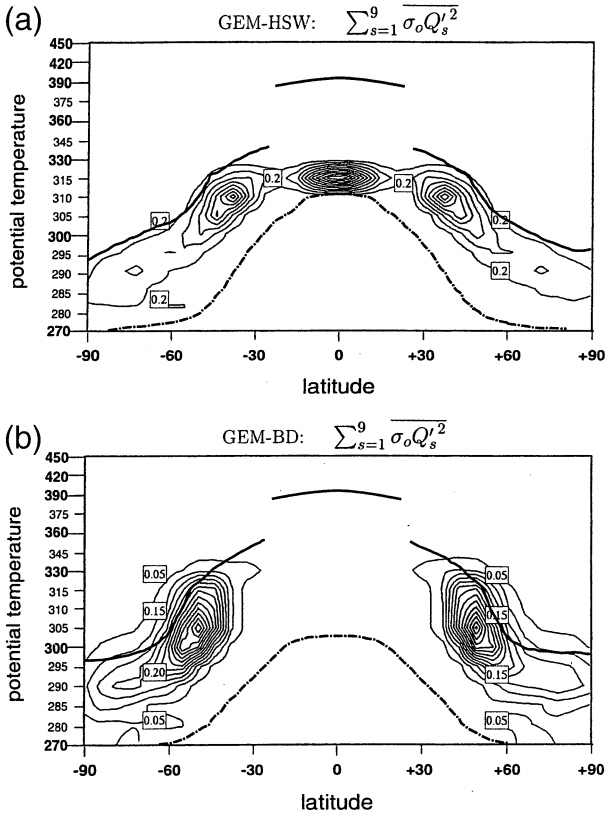

FIG. 5. Time-zonal mean of the (quasigeostrophic) enstrophy of transients, $\Sigma_{s=1}^{9}\sigma_o\overline{Q'^2_s}$ (3.9×10^{-7} kg m^{-2} K^{-1} s^{-2}) (a) with the HSW forcing and (b) with the BD forcing.

between energy and Doppler terms, when pseudoenergy virtually vanishes but pseudomomentum does not. If linear theory applies, these transition modes should be quasi-stationary.

Despite the generally consistent picture described above, there are differences in the wave-activity amplitudes and energy partition of the two experiments for the leading modes.

- The amplitudes of pseudomomentum and pseudoenergy are generally higher in the HSW experiment (Fig. 7) than in the BD experiment (Fig. 8). These relatively large amplitudes of pseudoenergy in the HSW experiment are due to low levels of kinetic and potential energy; recall that pseudoenergy is given by the difference between the energy and the Doppler terms. The energy amplitudes generated by the BD forcing are closer to those obtained with the NCEP data.
- In the HSW experiment, potential energy is larger than the kinetic component for wavenumbers $s < 5$ (Fig. 11a). Energy equipartition occurs near $s = 5$ (Fig. 11b), and kinetic energy only begins to lead at larger wavenumbers (Fig. 11c). Although the tendency is the same—that is, a kinetic-to-potential energy ratio increasing with wavenumbers—equipartition does not happen at the same scales observed in the real atmosphere (see Z2002).
- Using the BD forcing, we find an approximate equipartition between kinetic and potential energy for wavenumber $s = 1$ (Fig. 12a), with the kinetic term becoming gradually dominant as s increases (Figs. 12b and 12c). This is the same behavior observed in the diagnosis of the NCEP reanalysis data.

This difference may be explained by the way that thermal energy is controlled by the two forcings. In the HSW experiment, there is a relatively strong relaxation acting on the total temperature field (zonal-mean component as well as higher wavenumbers) and probably influencing the cascade and energy partition in normal-mode space. The BD forcing, on the other hand, only acts on the zonal-mean temperature, with a constant heating function and a weak relaxation, so that wave-activity partition in the rest of the spectrum is driven by the internal dynamics alone. The impact of these differences on the energy spectrum can also be observed, to some extent, in the slope of inertial subranges as given by Table 1.

Quasigeostrophic (QG) ondulatory properties provide yet another clue to the origin of the different partitions of eddy energy. Planetary waves in the QG midlatitude theory satisfy the condition (kinetic energy)/(potential energy) $= \kappa_H^2 a_R^2$, where $K_H^2 = k^2 + l^2$ is the horizontal wavenumber and a_R is the Rossby radius [see Gill (1982), chapter 12]. The Rossby radius is here defined as a property of the basic state; for instance, it may be defined as $a_R^2 = gH/f_o^2$, where H is the characteristic height scale or mean depth of the basic state. For a fixed horizontal wavenumber, and when the above relation holds, the energy partition will be different for basic states with different Rossby radii. In sum, it is likely that the difference between basic states in the HSW and BD experiments, due to different thermal relaxations, is partly responsible for the distinct energy partitions of modes.

d. Characteristic periods

Theoretical and observed periods of some leading ENMs, as defined in section 2c, are given in Table 2 for wavenumbers $s = 1$, 5, and 9. Mean frequencies and the associated observed periods are derived from the power spectrum of ENM pairs, assuming that the modes n and $n + 1$ pair off as components of a propagating mode (see Z2002 for details on this pairing method). A simple cross-spectral test may be used to verify this assumption: let $\tilde{a}_m(\omega)$ and $\tilde{a}_n(\omega)$ represent the complex Fourier transforms of a pair of time series, and define the power-spectrum correlation

$$\mathrm{PSC} = \frac{\langle|\tilde{a}_m|^2|\tilde{a}_n|^2\rangle}{\langle|\tilde{a}_m|^4\rangle^{1/2}\langle|\tilde{a}_n|^4\rangle^{1/2}},$$

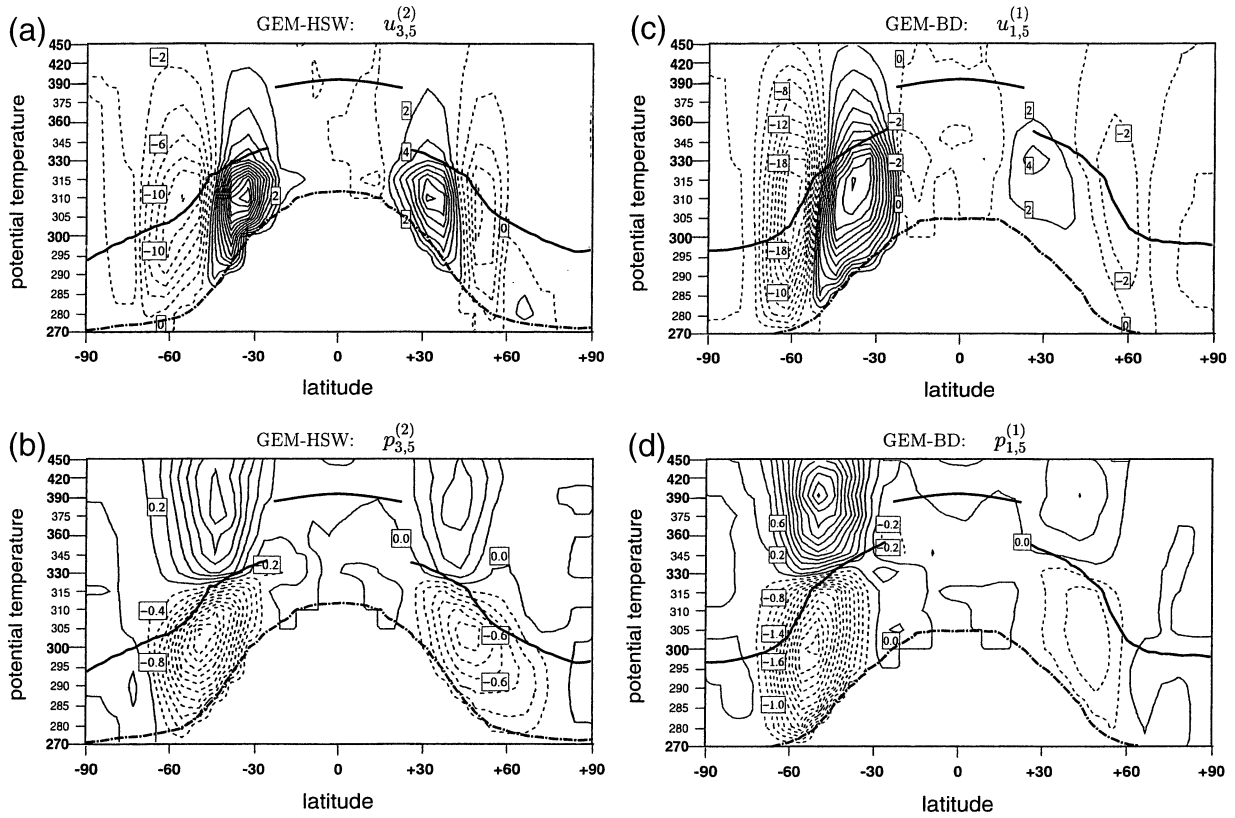

FIG. 6. Meridional cross sections showing the cosine component of the leading wavenumber-5 ENM of (a) zonal wind and (b) pressure in the HSW experiment and (c) zonal wind and (d) pressure in the BD experiment. Amplitudes are normalized by the basic fields according to Eq. (4) to provide local contributions to the pseudoenergy: winds are multiplied by $\alpha_o^{-1/2}$, and pressure is multiplied by $(\lambda p_o^{-k})^{1/2}$.

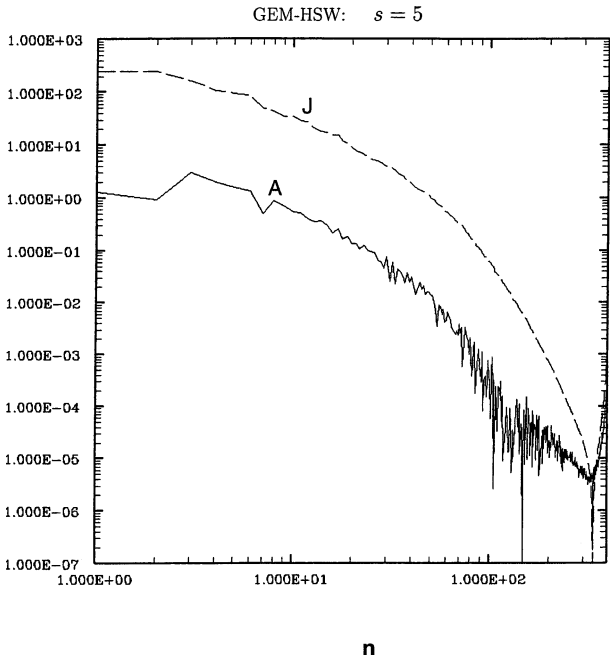

FIG. 7. Wave-activity spectra in the HSW experiment: Plot shows the absolute values of total pseudomomentum J (2.70×10^3 kg m^{-1} s^{-1}) and pseudoenergy A (1.25×10^6 J m^{-2}) with zonal wavenumber $s = 5$.

where brackets indicate average in frequency space. Also define the relative phase at peak frequency ω_p as

$$\Delta\alpha_{mn} = \alpha_m - \alpha_n, \qquad \sin\alpha_m = \frac{\mathrm{Im}[\tilde{a}_m(\omega_p)]}{|\tilde{a}_m(\omega_p)|}.$$

A propagating pair should have highly correlated power spectra and a relative phase near 90°, that is, $|\sin\Delta\alpha| \rightarrow 1$. Table 3 shows results of this analysis applied to various pairs of ENMs.

For the largest zonal scale ($s = 1$) we find some large theoretical periods (Table 2), sometimes on the order of hundreds of days. Unless the corresponding ENM pair is correctly separated, these large periods are difficult to obtain from the power spectrum approach, as has been observed in previous studies (Brunet and Vautard 1996; Z2002).

At sufficiently large wavenumbers (usually at $s \geq 5$), the power spectra tend to be more monochromatic and agreement between theoretical and observed periods increases. This behavior is also consistent with the results from the NCEP reanalysis study.

For the small-amplitude ENMs found in the large-n range of the spectrum, there is no agreement between observed and theoretical periods, either in the HSW or in the BD experiment—or in the reanalysis data study,

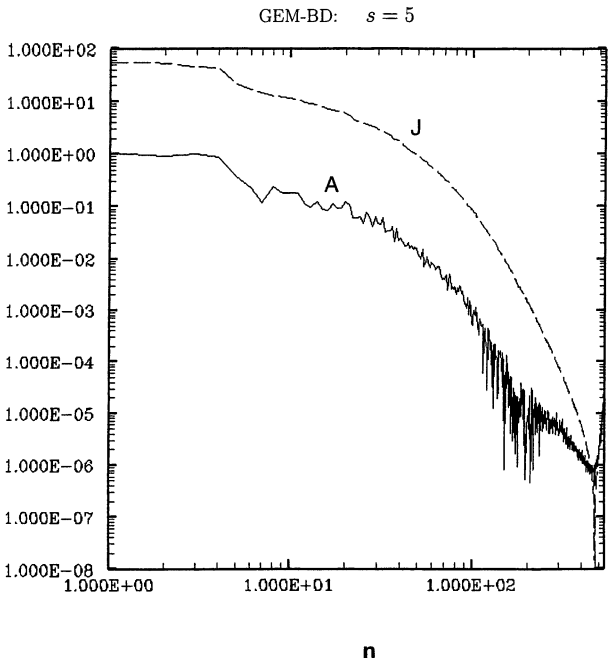

FIG. 8. As in Fig. 7, but using the BD forcing.

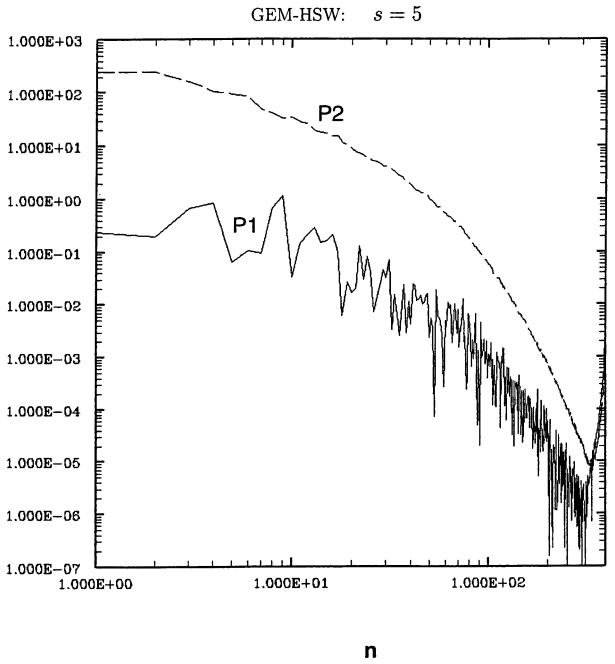

FIG. 9. Partition of pseudomomentum in the HSW experiment, in terms of the momentum (P1) and PV terms (P2) according to Eq. (3), for zonal wavenumber $s = 5$. Plot shows absolute values in units of 2.70×10^3 kilograms per meter per second.

for that matter. This mismatch may be attributable to the typically small amplitudes and small scales of modes in this range.

5. Summary and conclusions

A diagnostic study of the GEM model's dynamical core was presented, based on two experiments with different forcings. The ENM algorithm (Z2002) was used to characterize the climatology and the variability of the model's upper troposphere and lower stratosphere. As compared with other decomposition techniques, such as empirical orthogonal function analysis, the ENM method has the advantage of being rooted in linear dynamics, which allows the recognition and classification of propagating wavelike disturbances. This technique may now be applied to other models and results may be compared with those of the GEM model. We thus propose the ENM algorithm as a complementary tool to current methods used in intercomparison of atmospheric models.

Regardless of the idealized forcing used, results show that most wave activity in the model's upper troposphere and lower stratosphere is carried by eastward propagating disturbances, mainly at mid- and high latitudes. For some of the leading ENMs, with zonal wavenumbers larger than $s = 5$, the observed mean period approaches the theoretical value derived from the mode's spatial properties. Such matching of periods in nonlinear regimes had already been observed by Brunet and Vautard (1996) in experiments with a shallow-water model.

The diagnosis also reveals some important differences resulting from the choice of forcing. The temporal and zonal average fields obtained in the BD experiment show pressure gradients and midlatitude jets that resemble the summer-hemisphere fields obtained with reanalysis data, although the lower-stratosphere equatorial jet is unrealistically strong. The climatology generated

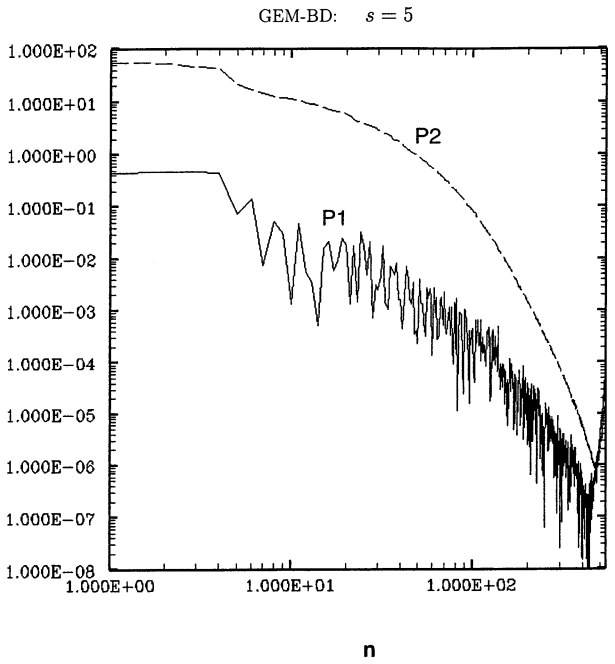

FIG. 10. As in Fig. 9, but using the BD forcing.

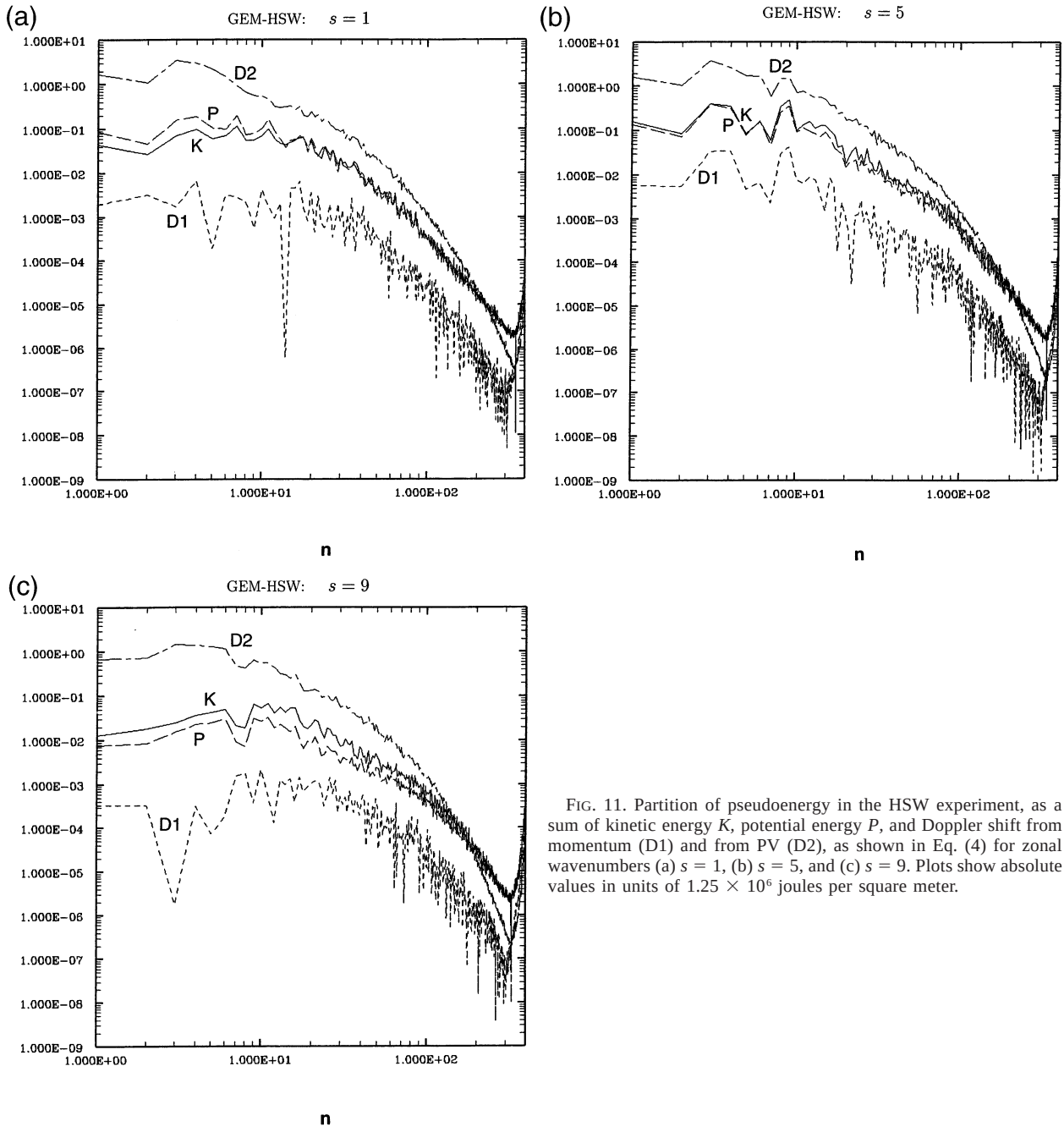

FIG. 11. Partition of pseudoenergy in the HSW experiment, as a sum of kinetic energy *K*, potential energy *P*, and Doppler shift from momentum (D1) and from PV (D2), as shown in Eq. (4) for zonal wavenumbers (a) $s = 1$, (b) $s = 5$, and (c) $s = 9$. Plots show absolute values in units of 1.25×10^6 joules per square meter.

with the HSW forcing produces a shallower troposphere, at least from the viewpoint of isentropic coordinates. A careful analysis of the ENM's pseudoenergy spectrum as a function of wavenumber also reveals that amplitude and partition of eddy energy are different in the two experiments, which is likely attributable to the difference between the thermal-energy relaxations prescribed in the two forcings.

As an attempt to measure the realism of the results, we have compared them with those of a previous study on atmospheric reanalysis data. This comparison must, of course, be made with caution because analyzed data are subject to effects, such as topography, land–sea contrast, and seasonal dependence, that are absent in the dynamical-core experiments. However, some features of the upper atmosphere's climatology and variability are sufficiently robust, and many characteristics of mean fields and disturbances are shared by the model and reanalysis data. In particular, the spatial structure and propagation properties of some of the most energetic ENMs in the dynamical-core experiments are remarkably similar to those obtained with the NCEP data. The

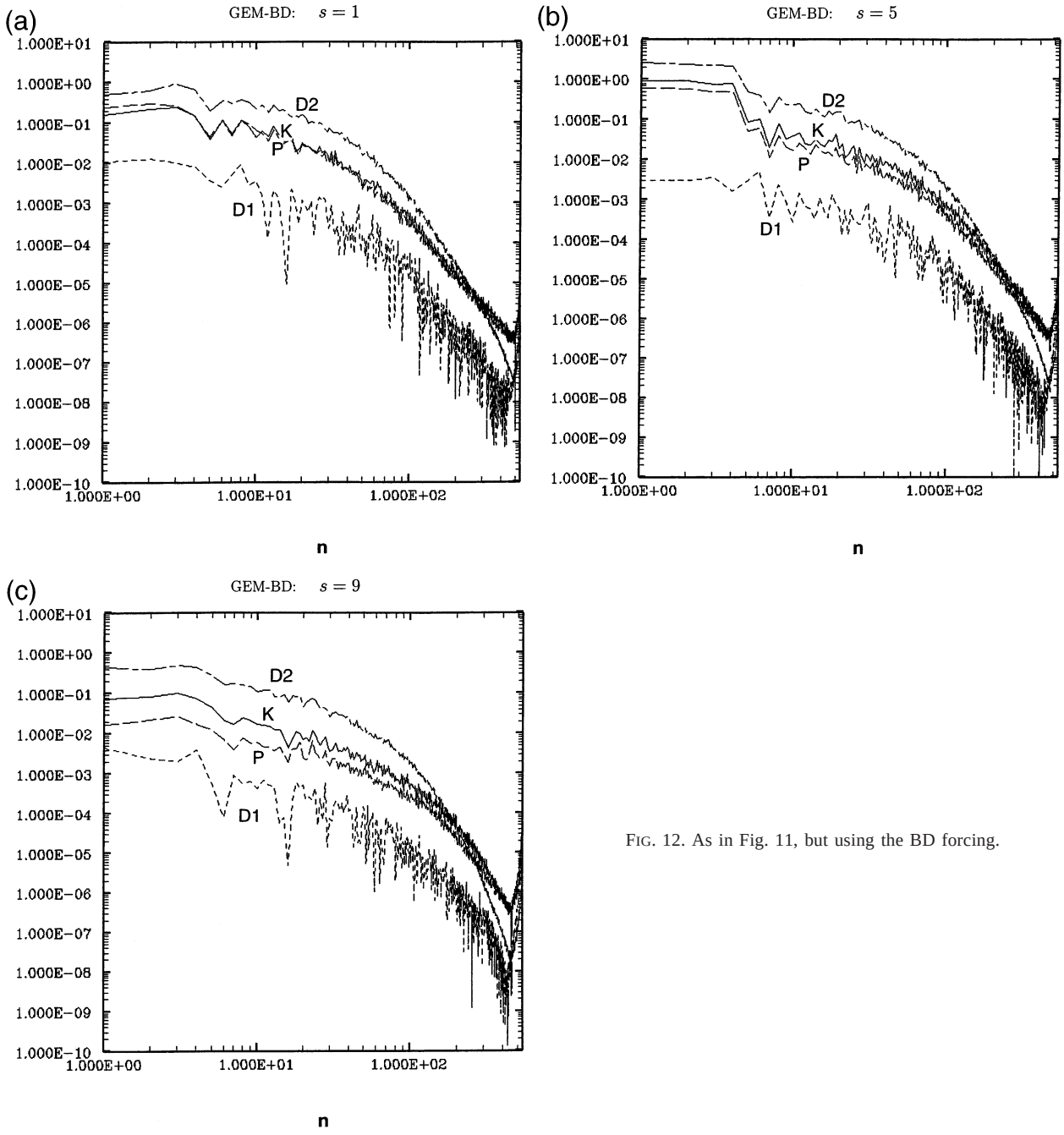

FIG. 12. As in Fig. 11, but using the BD forcing.

TABLE 1. Exponents b and d obtained from power-law fits of the kinetic energy $E_{\text{kin}} \sim n^{-b}$ and potential energy $E_{\text{pot}} \sim n^{-d}$ in two different subranges of the ENM indedx n for wavenumbers $s = 1$, 5, and 9.

		$s = 1$		$s = 5$		$s = 9$	
		HSW forcing	BD forcing	HSW forcing	BD forcing	HSW forcing	BD forcing
Small-n subrange	b	2.3	1.4	2.2	1.4	2.1	1.8
	d	2.5	1.5	2.2	1.5	1.8	1.8
Intermediate-n subrange	b	4.3	4.2	4.7	4.9	5.0	6.0
	d	4.2	4.2	4.5	4.7	4.6	5.3

TABLE 2. Observed (T_{obs}, c_{obs}) and theoretical (T_{th}, c_{th}) values of the mean period in days, and phase speed in meters per second, of some leading modes with wavenumbers $s = 1$, 5, and 9.

HSW forcing						BD forcing					
s	n	T_{obs}	T_{th}	c_{obs}	c_{th}	s	n	T_{obs}	T_{th}	c_{obs}	c_{th}
1	2	138	124	3	4	1	2	275	156	2	3
1	4	61	55	8	8	1	9	147	126	3	4
1	6	18	68	26	7	1	14	176	79	3	6
1	9	64	76	7	6	1	17	70	92	7	5
1	14	35	69	13	7	1	20	99	71	5	7
5	1	71	44	1	2	5	1	9	11	11	9
5	3	15	11	6	9	5	3	9	9	10	10
5	5	19	12	5	7	5	5	12	13	8	7
5	7	19	21	13	5	5	8	11	12	8	8
5	11	5	12	18	8	5	10	16	17	6	5
5	19	26	12	4	8	5	17	10	11	9	8
9	1	20	25	3	2	9	1	5.1	4.4	10	12
9	4	8.5	5.4	6	10	9	2	4.8	5.0	11	10
9	7	17	10	3	5	9	4	4.7	3.6	11	14
9	9	2.0	4.6	26	11	9	7	4.3	5.5	12	9
9	14	10.9	4.9	5	10	9	14	5.6	5.6	9	9
9	19	8.7	6.7	6	8	9	17	3.3	4.5	16	11

detailed wave-activity spectrum and other properties of climatology and wave propagation suggest, however, that the BD prescription (in which only the zonal mean component of temperature is forced) is the one that produces the more realistic results.

All of the above conclusions apply to the upper troposphere and lower stratosphere only. This paper must be seen as a complementary, not a complete, study of the variability in the GEM model's dynamical core. To diagnose the lower troposphere, a vertical coordinate other than potential temperature is advisable. This would require some modifications in the algorithm, mainly in the correlation matrix and surface contributions, which is feasible in principle. Also, topography might be added to the forcing to induce a more realistic behavior in the lower regions. In this case, a nonzonally symmetric basic state might be considered.

An immediate extension of this study would be a diagnosis of the model's upper stratosphere, where isentropic coordinates are still convenient and no modifications to the algorithm would be needed. In addition, ENM analysis could be used in an attempt to clarify properties of stratosphere–troposphere coupling. These extensions are proposed as work for the future.

TABLE 3. Examples of (i) power-spectrum correlation (PSC) between pairs (m, n) or time series and (ii) absolute value of the sine of relative phase $\Delta\alpha_{mn}$, evaluated near the power-spectrum peak frequency. Here s = zonal wavenumber and m, n = ENM numbers. When the PSC is high and $|\sin\Delta\alpha|$ approaches 1, the ENM pair is expected to behave as a propagating mode.

HSW forcing				BD forcing			
s	(m, n)	PSC (%)	$\lvert\sin\Delta\alpha_{mn}\rvert$	s	(m, n)	PSC (%)	$\lvert\sin\Delta\alpha_{mn}\rvert$
1	(4, 5)	79	0.94	1	(9, 10)	88	0.99
1	(9, 10)	84	0.97	1	(14, 15)	74	0.97
5	(3, 4)	74	0.94	5	(1, 2)	84	0.90
5	(5, 6)	84	0.99	5	(3, 4)	78	0.97
9	(1, 2)	99	1.00	9	(1, 2)	57	0.83
9	(7, 8)	87	0.97	9	(14, 15)	53	0.90

Acknowledgments. Author AZ thanks P. Bartello for helpful discussions and acknowledges support from the McGill University's Faculty of Graduate Studies and Research, the ''Fonds pour la Formation de Chercheurs et l'Aide à la Recherche du Québec,'' and the Meteorological Service of Environment Canada. The authors also thank an anonymous reviewer for suggesting the cross-spectral diagnosis of propagating pairs.

APPENDIX

Note on the Snapshot Method

A proof is given that the snapshot method, as defined by the real eigenvalue problem in Eqs. (6)–(7), can determine the two separate phases of a propagating mode in the linear limit. Let us consider the complex representation of normal modes:

$$\mathbf{X} = \begin{pmatrix} u \\ \sigma \\ q \end{pmatrix} = \mathrm{Re} \sum_{s=0}^{\infty} \mathbf{X}_s(\phi, \theta, t) e^{is\lambda},$$

$$\mathbf{X}_s(\phi, \theta, t) = \sum_n a_{ns}(t)\mathbf{X}_{ns}(\phi, \theta). \tag{A1}$$

In the linear case, $a_{ns}(t) = e^{-i\omega_{ns}t}$ and, provided the frequency spectrum is nondegenerate and all modes are neutral, the conservation of pseudomomentum implies the orthogonality relation $\langle \mathbf{X}_{ms}, \mathbf{X}_{ns} \rangle \propto \delta_{mn}$ (Held 1985), where the pseudomomentum norm is used to define

$$\langle \mathbf{X}, \mathbf{Y} \rangle = 2\pi a^2 \int d\theta\, d\phi\, \cos\phi \mathbf{X}^{t*} B \mathbf{Y},$$

$$B = \frac{\cos\phi}{2} \begin{pmatrix} 0 & 1 & 0 \\ 1 & 0 & 0 \\ 0 & 0 & -\sigma_o^2/\gamma_o \end{pmatrix}. \tag{A2}$$

Using this orthogonality relation and normalizing the modes such that $\langle \mathbf{X}_{ms}, \mathbf{X}_{ns} \rangle = \lambda_{ns}\delta_{mn}$ and $\overline{a_{ms}^* a_{ns}} = \delta_{mn}$, it is readily shown that the complex principal components a_{ns} must solve the eigenvalue equation

$$\frac{1}{T} \int_0^T dt'\, \tau_s(t, t') a_{ns}^*(t') = \lambda_{ns} a_{ns}^*(t),$$

$$\tau_s(t, t') = \langle \mathbf{X}_s(t), \mathbf{X}_s(t') \rangle \tag{A3}$$

for all values of s. Note that this is not the same equation as in Eq. (6), because here τ_s is the complete, complex time-covariance operator. To compare the real and complex formulations of the problem, let us expand the complex operator as

$$\tau_s(t, t') = \sum_{m,n} a^*_{ms}(t)a_{ns}(t')\langle \mathbf{X}_{ms}, \mathbf{X}_{ns}\rangle = \sum_n \lambda_{ns}a^*_{ns}(t)a_{ns}(t') \quad \text{(A4)}$$

and write its real and imaginary parts as

$$\tau^R_s(t, t') = \sum_n \lambda_{ns}[a^R_{ns}(t)a^R_{ns}(t') + a^I_{ns}(t)a^I_{ns}(t')] \quad \text{and} \quad \text{(A5)}$$

$$\tau^I_s(t, t') = \sum_n \lambda_{ns}[a^R_{ns}(t)a^I_{ns}(t') - a^I_{ns}(t)a^R_{ns}(t')]. \quad \text{(A6)}$$

In the linear limit, the real and imaginary parts of a_{ns}, typically given by $\cos\omega_{ns}t$ and $\sin\omega_{ns}t$, obey the orthogonality relations $\overline{a^R_{ms}a^R_{ns}} = (1/2)\delta_{mn} = \overline{a^I_{ms}a^I_{ns}}$ and $\overline{a^R_{ms}a^I_{ns}} = 0$. It follows that the real and imaginary parts of the PCs are degenerate eigenvectors of the real part of the τ_s:

$$\frac{1}{T}\int_0^T dt'\ \tau^R_s(t, t')a^R_{ns}(t') = +\frac{\lambda_{ns}}{2}a^R_{ns}(t) \quad \text{and} \quad \text{(A7)}$$

$$\frac{1}{T}\int_0^T dt'\ \tau^R_s(t, t')a^I_{ns}(t') = +\frac{\lambda_{ns}}{2}a^I_{ns}(t). \quad \text{(A8)}$$

Equation (6) is the discrete version of the eigenvalue problem above. It involves just the real part of τ_s but is sufficient to generate all PCs. The imaginary part of τ_s only transforms the real and imaginary parts of the PCs into each other:

$$\frac{1}{T}\int_0^T dt'\ \tau^I_s(t, t')a^R_{ns}(t') = -\frac{\lambda_{ns}}{2}a^I_{ns}(t) \quad \text{and} \quad \text{(A9)}$$

$$\frac{1}{T}\int_0^T dt'\ \tau^I_s(t, t')a^I_{ns}(t') = +\frac{\lambda_{ns}}{2}a^R_{ns}(t). \quad \text{(A10)}$$

Notice that the set of Eqs. (A7)–(A10) imply the complex eigenvalue problem in Eq. (A3).

REFERENCES

Boer, G. J., and B. Denis, 1997: Numerical convergence of the dynamics of a GCM. *Climate Dyn.*, **13,** 359–374.

Brunet, G., 1994: Empirical normal-mode analysis of atmospheric data. *J. Atmos. Sci.,* **51,** 932–952.

——, and R. Vautard, 1996: Empirical normal modes versus empirical orthogonal functions for statistical prediction. *J. Atmos. Sci.*, **53,** 3468–3489.

Côté, J., J.-G. Desmarais, S. Gravel, A. Méthot, A. Patoine, M. Roch, and A. Staniforth, 1998a: The operational CMC–MRB Global Environmental Multiscale (GEM) model. Part I: Design considerations and formulation. *Mon. Wea. Rev.*, **126,** 1373–1395.

——, S. Gravel, A. Méthot, A. Patoine, M. Roch, and A. Staniforth, 1998b: The operational CMC–MRB Global Environmental Multiscale (GEM) model. Part II: Results. *Mon. Wea. Rev.*, **126,** 1397–1418.

Gill, A. E., 1982: *Atmosphere–Ocean Dynamics.* Academic Press, 662 pp.

Held, I. M., 1985: Pseudomomentum and the orthogonality of modes in shear flows. *J. Atmos. Sci.*, **42,** 2280–2288.

——, and M. J. Suarez, 1994: A proposal for the intercomparison of the dynamical cores of atmospheric general circulation models. *Bull. Amer. Meteor. Soc.*, **75,** 1825–1830.

Hoskins, B. J., and D. Karoly, 1981: The steady linear response of a spherical atmosphere to thermal and orographic forcing. *J. Atmos. Sci.*, **38,** 1179–1196.

Rivest, C., and B. F. Farrell, 1992: Upper-tropospheric synoptic-scale waves. Part II: Maintenance and excitation of quasi modes. *J. Atmos. Sci.*, **49,** 2120–2138.

——, C. A. Davis, and B. F. Farrell, 1992: Upper-tropospheric synoptic-scale waves. Part I: Maintenance as Eady normal modes. *J. Atmos. Sci.*, **49,** 2108–2119.

Sirovich, L., and R. Everson, 1992: Management and analysis of large scientific datasets. *Int. J. Supercomp. Appl.*, **6** (1), 50–68.

Williamson, D. L., J. G. Olson, and A. B. Byron, 1998: A comparison of semi-Lagrangian and Eulerian tropical climate simulations. *Mon. Wea. Rev.*, **126,** 1001–1012.

Zadra, A., 2000: Empirical normal mode diagnosis of reanalysis data and dynamical-core experiments. Ph.D. Thesis, McGill University, Montreal, Quebec, Canada, 221 pp.

——, G. Brunet, and J. Derome, 2002: An empirical normal mode diagnostic algorithm applied to NCEP reanalyses. *J. Atmos. Sci.*, in press.